WILEY-VCH

Electrically Tunable and Modulated Perovskite Quantum Emitters via Surface-Enhanced Landau Damping

Yan Liu[1,2], Jun Zhang[1], Evelin Csányi[1], Nur Qalishah Adanan[3], Hongtao Wang[3], Zheng Zhang[1], Sherry Lee Koon Yap[1], Henry Yit Loong Lee[1], Shutao Zhang[1,3], Wei Peng Goh[1], Li Jun Lim[4], Zhi-Kuang Tan[4], Jian Rui Soh[1], Lulu Xiong[5], Dmitry A. Kalashnikov[1], Robert E. Simpson[3,6], Cheng-Wei Qiu[7], N. Asger Mortensen[8,9], Joel K. W. Yang[3,] and Zhaogang Dong[1,2,3*]*

[1]Institute of Materials Research and Engineering (IMRE), Agency for Science, Technology and Research (A*STAR), 2 Fusionopolis Way, Innovis #08-03, Singapore 138634, Republic of Singapore

[2]Quantum Innovation Centre (Q. InC), Agency for Science Technology and Research (A*STAR), 2 Fusionopolis Way, Innovis #08-03, Singapore 138634, Republic of Singapore

[3]Singapore University of Technology and Design, 8 Somapah Road, 487372, Singapore

[4]Department of Chemistry 3 Science Drive 3, National University of Singapore, 117543, Singapore

[5]Institute of Applied Physics and Materials Engineering, University of Macau, Avenida da Universidade, Taipa, Macau, 999078, China

[6]Department of Electronic, Electrical and Systems Engineering School of Engineering, University of Birmingham, Edgbaston, Birmingham, B15 2TT, United Kingdom

[7]Department of Electrical and Computer Engineering National University of Singapore 4 Engineering Drive 3, Singapore 117583, Singapore

[8]POLIMA–Center for Polariton-driven Light Matter Interactions, University of Southern Denmark Odense DK-5230, Denmark

[9]Danish Institute for Advanced Study, University of Southern Denmark, DK-5230 Odense, Denmark

*Correspondence and requests for materials should be addressed to Z.D. (email: zhaogang_dong@sutd.edu.sg) and J.K.W.Y. (email: joel_yang@sutd.edu.sg).

Keywords: Phase-change materials, Localized surface plasmons (LSPs) excited hot-electron injection, surface-enhanced Landau damping, Electrical modulation, Tunable perovskite quantum emissions

Tuning quantum emission to a specific wavelength at room temperature holds significant promise for enhancing secure quantum communication, particularly by aligning with the Fraunhofer lines in the solar spectrum. The integration of quantum emitters with phase-change materials enables emission wavelength modulation, especially when strong field enhancement is present. Antimony telluride (Sb_2Te_3) exhibits the potential to facilitate this functionality through its support of interband plasmonics and phase-change behavior. In this study, we designed and fabricated Sb_2Te_3 antennae capable of tuning the emission energy of adjacent perovskite quantum dots (QDs) by over 570 meV. The underlying mechanism involves the localized surface plasmons (LSPs) on Sb_2Te_3 nanostructures, which exhibit a surface-enhanced Landau damping process that facilitates the decay of LSPs into electron-hole pairs. The generated hot electrons are then injected into perovskite QDs via the microscopic electron transport process, which can be trigged by the transition of Sb_2Te_3 from amorphous to crystalline state, resulting in a significant emission energy shift from 1.64 eV to 2.21 eV. Furthermore, the emission energy of perovskite QDs on crystalline Sb_2Te_3 nanoantennae can be modulated through DC voltage bias, highlighting the potential for extensive wavelength tunability of quantum emitters integrated with electronic systems.

1. Introduction

Manipulating and controlling the characteristics of light emission, including amplitude[1], phase[2], polarization,[3] directionality,[4] and wavelength,[5] is foundational in optical information encryption.[6] Among these dimensions, in-situ control of the light emission wavelength, such as tunable laser sources and single photon emitters, is pivotal for various applications, such as integrated quantum photonics, [7] quantum communication,[8] neuromorphic computing,[9] reconfigurable imaging[10], reconfigurable quantum circuits,[11] optical information processing,[12] and optical network switching.[13] The techniques for achieving tunable emission wavelength typically relies on the stimuli of extremely strong electric/magnetic fields, high pressure, or low temperature with sophisticated and often bulky apparatus, limiting their potential applications for energy-efficient integrated photonics.

On the other hand, coupling quantum dots (QDs) with optical nanoantenna offers a promising approach towards achieving tunable emitters with compact footprints, leveraging the strong Purcell effect. Thus far, significant efforts have been carried out to develop reconfigurable optical nanoantenna, enabling the manipulation of its reflection/transmission spectra via electro-optical,[14] thermo-optical[15], mechano-optical,[16] and phase-change materials.[15b, 17] However, the proof-of-concept of coupling quantum emitters to nanoantenna with spectral tunability has not been fully explored yet. So far, for instance, a polarization controlled quasi bound-states-in-the-continuum (q-BIC) nanoantenna is able to moderately tune the emission wavelength of perovskite QDs by ~10 nm (≈ 20 meV). [5a] Therefore, an optical nanoantenna capable of tuning the emission wavelength with spectral shift of hundreds of meV remains highly desirable integrated quantum photonics.

Antimony telluride (Sb_2Te_3), belonging to the *p*-block group of elements, is an emerging phase-change material platform that provides multiple functionalities, *i.e.*, interband transition in plasmonics, topological insulators, and thermoelectrics. Such multifunctionalities have led to applications in photodetection,[18] microelectronics,[19] and energy harvesting.[20] Compared to conventional plasmonic materials, e.g., gold (Au),[21] and silver (Ag),[22] Sb_2Te_3 can provide greater

flexibility and new opportunities in the design of plasmonic applications. For example, it is able to provide more degree-of-freedoms for interband plasmonics with its tunable refractive index and energy band structures.[23] In another perspective, crystalline state Sb_2Te_3 is a well-known topological insulator, as the surface states residing in the bulk insulating gap of such system [24] are conductive. It has unique electronic properties where the bulk of the material acts as an insulator, but its surface conducts electricity due to the presence of special surface states. The top surface of the topological insulator Sb_2Te_3 can indeed host hot-electrons. These hot electrons are high-energy carriers that can be generated through various processes, such as optical excitation or electrical biasing[25]. Further possibilities could be explored in combination with other bismuth and antimony chalcogenides, such as $Bi_{1.5}Sb_{0.5}Te_{1.8}Se_{1.2}$,[26] Bi_2Te_3,[27] and Bi_2Se_3[28]. Nevertheless, these unique characteristics of phase-change interband plasmonics, especially with hot-electron injection and tunable energy band structure, have not been explored thoroughly.

Perovskite QDs exhibit high quantum efficiency and narrow emission line width, making them ideal for light-emitting applications.[29] In particular, lead halide perovskites are widely used in nanophotonics due to their large optical absorption coefficient, efficient photocarrier extraction and light emission, and low synthesis cost. [30] The perovskite crystal structure follows the formula of $APbX_3$, where the perovskite QDs in this work is $CH(NH_2)_2PbI_3$ ($FAPbI_3$).[31] In this work, we demonstrate that the emission properties of $FAPbI_3$ perovskite quantum dots (QDs) can be dynamically tuned through integration with an electrically controlled, phase-change Sb_2Te_3 nanoantenna. The nanoantenna supports localized surface plasmons (LSPs) that undergo surface-enhanced Landau damping,[32] decaying into electron–hole pairs and generating a hot-electron population. These hot electrons are subsequently injected from the crystalline Sb_2Te_3 into the perovskite QDs via the microscopic electron transport process, thereby modifying QDs' emission wavelength from 1.64 eV to 2.21 eV, *i.e.*, an emission energy shift of 570 meV. Furthermore, we have also demonstrated the electrical tunability of this quantum emission energy over a range of 307 meV by modulating the charge-transfer process with a DC voltage

bias ranging from -4V to 4V. This advancement holds promise for applications in manipulating quantum emission, quantum computing, and ultrafast optical switching, especially with the integration of electrically switching circuit of Sb_2Te_3.[33]

2. Mechanism of electrically modulated and tunable perovskite quantum emissions via surface-enhanced Landau damping

Our strategy for electrically modulating and tuning quantum emission at room temperature involves integrating perovskite quantum emitters with phase-change Sb_2Te_3 nanoantennae via surface-enhanced Landau damping. This integration enables on-chip tuning of the perovskite quantum emission wavelength and modulation of quantum emission intensity. As shown in **Figure 1a**, our device consists of an optical silicon nanoantenna with a phase-change Sb_2Te_3 film covering its top surface. The nanoantenna is fabricated on a Si_3N_4/Si substrate, with perovskite quantum dots (QDs) evenly distributed across the optical antennae. A SiO_2 dielectric film is then deposited on the nanoantenna as an insulating layer between the top transparent indium tin oxide (ITO) electrode and the bottom p-Si substrate.

The photoluminescence (PL) of perovskite QDs can be excited by an external laser, with the emission peak wavelength tunable through the phase change of Sb_2Te_3. The quantum emission tuning mechanism relies on both microscopic electronic processes (hot-electron injection) and macroscopic resonance modifications (changes in the refractive index of the Sb_2Te_3 film), where the first mechanism is the dominating one. Additionally, applying an external DC voltage bias to the top ITO electrode, while grounding the *p*-Si substrate, allows modulation of the PL emission. The inset of Figure 1a illustrates that the perovskite QDs are coated not only on the top and sidewalls of the Sb_2Te_3 nanopillar but also on the Si_3N_4/Si substrate.

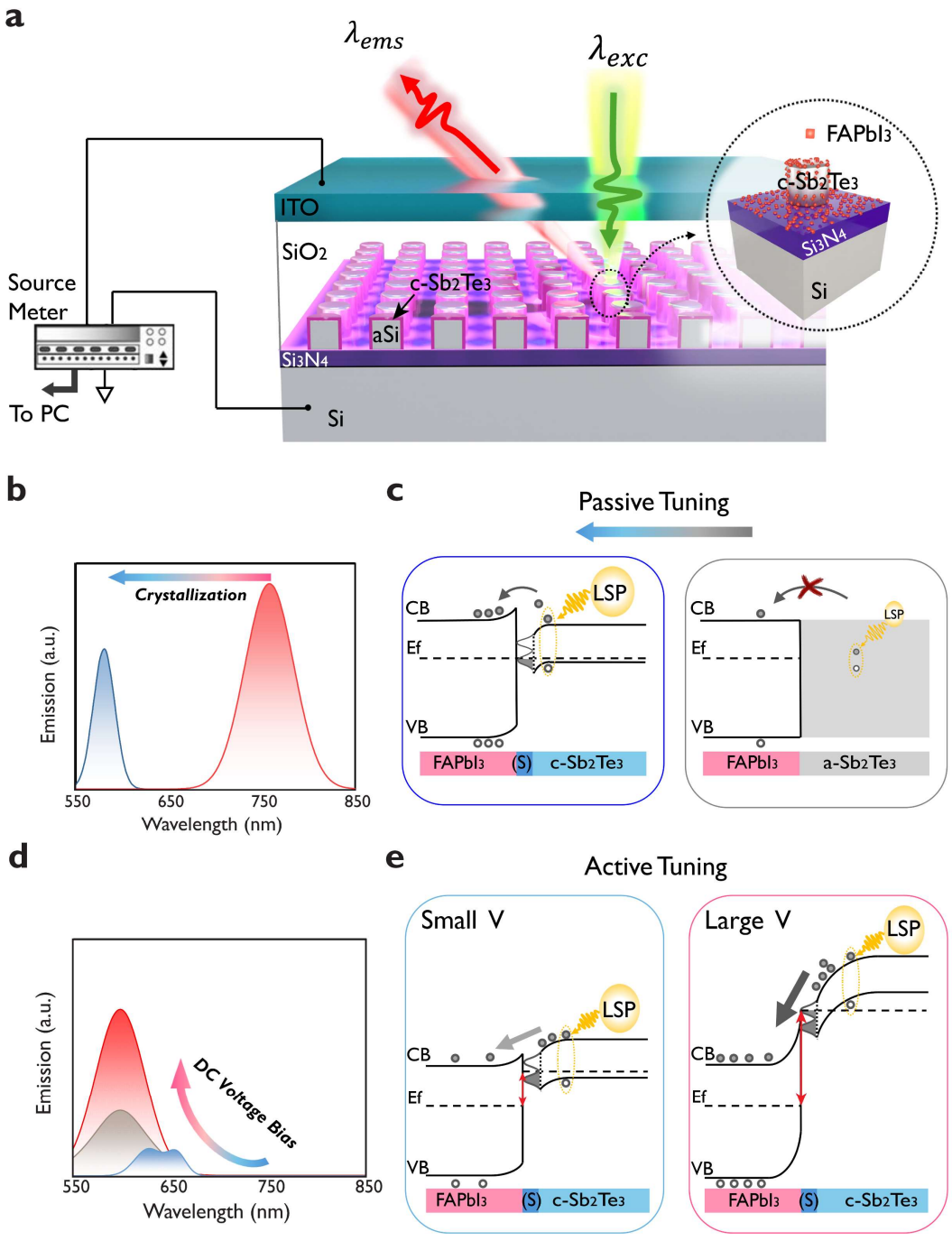

Figure 1 | Electrically tunable and modulated Sb_2Te_3 nanoantenna integrated with perovskite quantum emitters via surface-enhanced Landau damping and hot electron injection via the microscopic transport process. a, Schematic of the hybrid perovskite-Sb_2Te_3 nanostructure, where perovskite QDs are integrated with a phase-change nanoantenna between a *p*-type Si bottom layer and an ITO top electrode (see Figure 2a for details). **b,** Photoluminescence spectra demonstrating passive emission wavelength tuning. **c,** Equilibrium-state energy band diagram illustrating surface-enhanced

Landau damping and followed by the hot-electron injection via microscopic transport process from crystalline Sb_2Te_3 to perovskite QDs. In comparion, no microscopic electron transport is observed at $FAPbI_3$/a-Sb_2Te_3 interface when Sb_2Te_3 is in amorphous state. **d,** Photoluminescence spectra showing quantum emission modulation under an external voltage bias. **e,** Energy band diagram depicting voltage-dependent surface-enhanced Landau damping and electron transport process, where the population of hot-electron injection increases with respect to the rising positive bias.

Figure 1b illustrates the tunable quantum emissions from perovskite/Sb_2Te_3 nanoantennae, achieved through the activation of surface-enhanced Landau damping. This mechanism facilitates the excitation of hot electrons and holes, followed by hot-electron injection into perovskite QDs. **Figure 1c** presents the corresponding energy band diagram of the perovskite/ Sb_2Te_3 nanoantennae in the passive tuning mode (*i.e.*, without an external voltage bias), where the material phase of Sb_2Te_3 is changed from amorphous to crystalline. The high density of conductive surface states at the top surface of the c-Sb_2Te_3 layer (S) exhibits a gapless energy band structure. Furthermore, this surface-enhanced Landau damping effect can be modulated electrically by applying an external DC voltage bias. This modulation enables active tuning of quantum emission from the nanoantennae by controlling hot-electron injection under a DC voltage bias, as illustrated in **Figure 1d**. When a DC voltage bias is applied to the $FAPbI_3$ side, the surface band of c-Sb_2Te_3 bends downward further, leading to an accumulation of electrons at the top surface, as depicted in **Figure 1e**.

3. Perovskite QDs integrated onto phase-change Sb_2Te_3 nanoantenna with interband plasmonics.

In this section, we demonstrate the passive tunability of quantum emission via surface-enhanced Landau damping and followed by the hot electron injection into perovskite QDs via the microscopic transport process. To simplify the device structure of perovskite/Sb_2Te_3 nanoantennae, the investigation of passive tunning quantum emission begins with pure 150-nm-tall Sb_2Te_3 nanodisk array coated

with perovskite QDs, as shown in the schematic of **Figure 2a** (See *Method 8.1*). Here, the Sb_2Te_3 nanoantennae were patterned on top of a 70-nm silicon nitride (Si_3N_4) on silicon (Si) substrate using electron beam lithography (EBL), followed by dry etching and an annealing process to crystallize Sb_2Te_3 (see details in Supplementary Figure S1). The tilted SEM image of c-Sb_2Te_3 nanodisk array is presented in **Figure 2b**. The $FAPbI_3$ perovskite QDs has a bandgap of 1.64 eV, [5a] and a cube size ranging from 10~15 nm (see Supplementary Figure S2), enabling them to be fit in the gaps between the Sb_2Te_3 antennae. Note that prior to the drop casting of $FAPbI_3$ QDs onto the Sb_2Te_3 nanoantenna surface, we observed no PL emission from the bare Sb_2Te_3 nano disks (see Supplementary Figure S3).

The plasmonic characteristics of Sb_2Te_3 lie in the ultraviolet to visible range, which originates from interband transitions,[34] rather than free electrons[34b] as observed in traditional noble metals, such as gold (Au),[35] silver (Ag) [22] as well as aluminum (Al).[36] This interband transition in plasmonics arises from the nature of chemical bonding and crystallographic structure of Sb_2Te_3 (see Supplementary Figure S4), rendering it with a tunable and negative dielectric function (ε_1), *i.e.*, $\varepsilon_1 < 0$ (see Supplementary Figs. S5, S6 and S7.[23, 34b] As Sb_2Te_3 has a disordered structure in the amorphous state (a-Sb_2Te_3) and long-range ordered structure in crystalline state (c-Sb_2Te_3), the phase transition between the two directly affects its energy band diagram and refractive indices (n & k).[37] Consequently, the material exhibits distinct plasmonic properties in its crystalline and amorphous states. Numerical simulations of Sb_2Te_3 nanodisk arrays demonstrate that the localized surface plasmon (LSP) resonance of c-Sb_2Te_3 nanodisks manifests a significantly higher electric field enhancement ($|E/E_{inc}|$) in the gap regions, as compared to the amorphous state, as shown in **Figure 2c**. The corresponding charge distributions follow that of a signature dipolar plasmonic resonance in both phase states (**Figure 2d**). Density-functional theory (DFT) calculations has been carried out to obtain the energy band structure of bulk c-Sb_2Te_3 (see Supplementary Figure S8). Our results indicate a narrow band gap of ~0.3 eV at the Γ-point, which agrees well with the literature.[38] The c-Sb_2Te_3 possesses a metallic surface state and insulating bulk state, which have different optical properties [24]. The bulk Sb_2Te_3 material supporting

the thin film was modelled using the Tauc-Lorentz model that has been successfully applied to this phase change material, while electrical conductivity of the topological insulator film was assumed to obey the Drude model. From our data analysis of ellipsometry, the best-fit parameters such as band gap of the bulk component, 0.3 eV, thickness of the topological insulator layer, d=2 nm. The details of dielectric constant of surface and bulk c-Sb_2Te_3 fitting model are shown in Supplementary Figure S7. The corresponding plasmon frequency of bulk Sb_2Te_3 material and Sb_2Te_3 nanoantennae could be found in the literature[39].

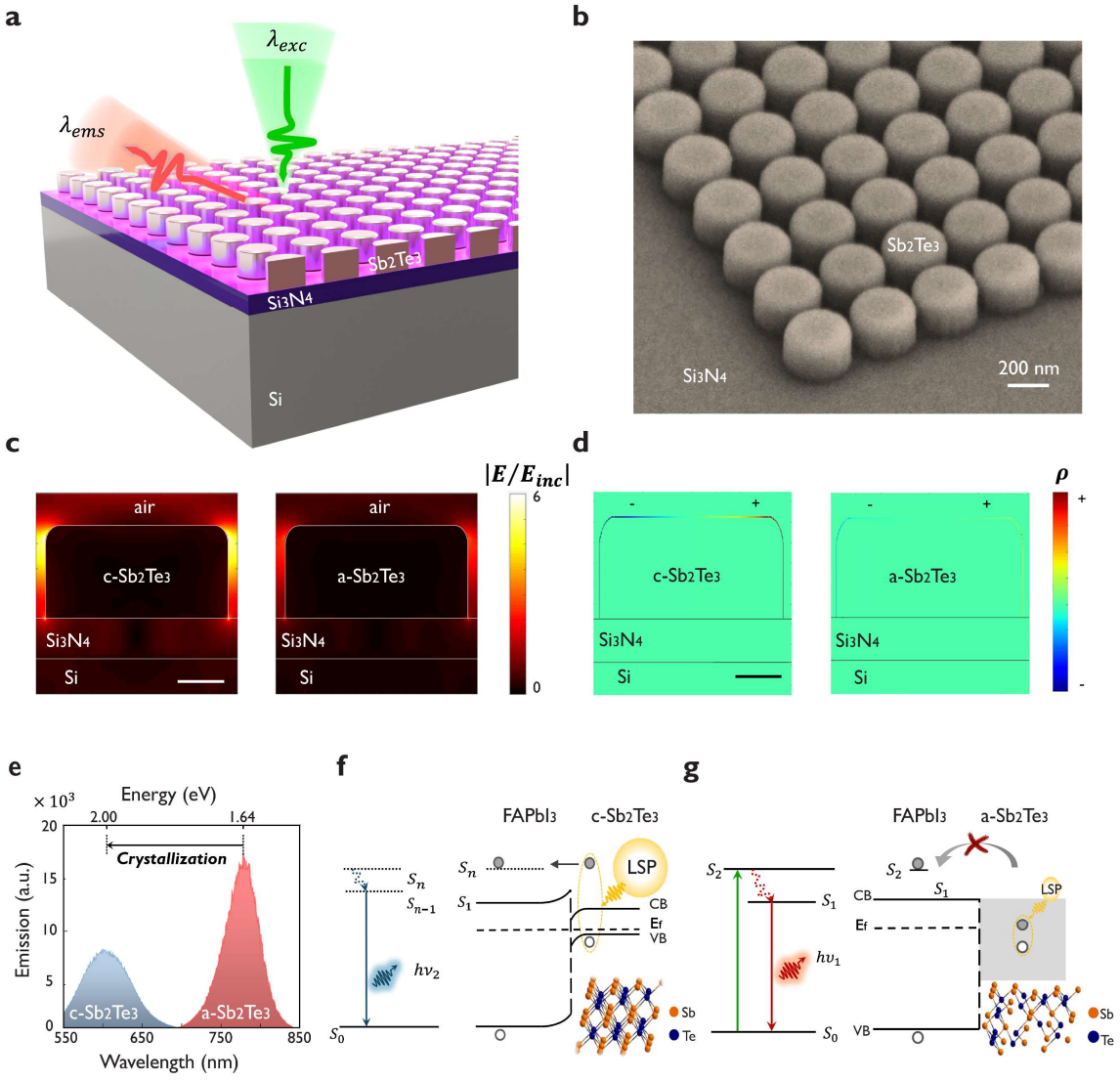

Figure 2 | Localized surface plasmon-enhanced Landau damping and hot electron injection on phase-change Sb_2Te_3 nanostructures for tunable PL emission from perovskite QDs. a, Schematic

of perovskite QDs integrated onto phase-change Sb_2Te_3 nanoantennae on an Si_3N_4/Si substrate. **b,** Tilted SEM image of crystalline Sb_2Te_3 (c-Sb_2Te_3) nanodisks without QDs. **c,** Simulated cross-sectional electric-field distributions ($|E/E_{inc}|$) for c-Sb_2Te_3 and amorphous Sb_2Te_3 (a-Sb_2Te_3) nanodisk arrays (scale bar: 100 nm). **d,** Simulated charge distribution of a dipole mode in c-Sb_2Te_3 and a-Sb_2Te_3 nanodisks (scale bar: 100 nm). **e,** PL spectra of perovskite QDs on Sb_2Te_3 nanodisks, showing a ~360 meV peak shift upon Sb_2Te_3 crystallization. **f**, Energy band diagram of $FAPbI_3$ QDs on c-Sb_2Te_3, where interband plasmons enhance Landau damping, generating hot electron-hole pairs. Hot electrons are then injected into $FAPbI_3$ QDs and decay from S_{n-1} to S_0 (2.0 eV). S_0, S_{n-1}, and S_n represent the ground, first excited, and second excited states, respectively. **g**, Energy band diagram of $FAPbI_3$ on (a-Sb_2Te_3), where excited electrons at the conduction band minimum decay from S_1 to S_0 (1.64 eV).

The photoluminescence (PL) spectra of perovskite QDs on amorphous and crystalline Sb_2Te_3 nanoantennae were recorded using a 532 nm continuous-wave (CW) pump laser and are shown in **Figure 2e**. This PL measurements were accomplished with the same sample before (amorphous state) and after (crystalline state) annealing process (see *Method 8.4*). Upon the phase change transition from amorphous to crystalline states, the PL emission peak shifts from 1.64 eV (~755 nm) to 2.00 eV (~617 nm). Thus, leveraging the phase change effect, this nano-system design enables a switchable photoluminescence (PL) energy ranging up to 360 meV, which is already unusually large compared to other tuning mechanisms characterized by sophisticated setups reported so far in Supplementary Figure S9. It is noted that the PL emission intensity is reduced when the perovskite is deposited on the crystalline nanodisk array, which could be attributed to non-radiative quenching effects of interband plasmonics in c-Sb_2Te_3.

Figures 2f and **2g** present a schematic of the respective electron energy band diagrams of perovskite QDs deposited onto crystalline and amorphous Sb_2Te_3 nanoantennae, illustrating the underlying hot-electron generation and injection mechanism that give rise to the wavelength shifting in

perovskite QDs emission. Although there are reports on hot-electron injection from conventional metallic nanostructures into semiconductors, [32d, 40] hot-electron injection excited by interband plasmons has not been investigated so far. We note that c-Sb_2Te_3 is a *p*-type semiconductor, while $FAPbI_3$ is close to an intrinsic semiconductor.[40] Thus, when c-Sb_2Te_3 and the $FAPbI_3$ perovskite QDs are in electrical contact as a straddling-gap heterojunction, the position of the energy minima of the significantly larger bandgap of $FAPbI_3$ allows the excess holes in c-Sb_2Te_3 to diffuse into $FAPbI_3$. Here, the straddling-gap heterojunction refers to that the bandgap of c-Sb_2Te_3 is completely contained in the one of $FAPbI_3$ perovskite QDs. At equilibrium, the built-in electric field pointing from perovskite QDs to Sb_2Te_3 prevents holes from further diffusion. As a result, c-Sb_2Te_3 will be negatively charged relative to the perovskite QDs at the interface.

Next, we discuss how the excitation of hot electron-hole pairs and injection of hot-electrons in $FAPbI_3$/c-Sb_2Te_3 enables the modulation of the QDs photoluminescence process (Figure 2f). It is summarized in the following 3 key steps:

(1) Microscopic resonances: When the 532 CW laser illuminates $FAPbI_3$/c-Sb_2Te_3 nanoantennae, it excites the localized surface plasmons (LSPs), which are supported on c-Sb_2Te_3 nanostructures. LSPs will consequently experience the surface-enhanced Landau damping to generate hot electron-hole pairs in c-Sb_2Te_3, across its relatively small bandgap (0.3 eV).

(2) Microscopic electron transport: Due to the built-in electric field at the interface of $FAPbI_3$/c-Sb_2Te_3, the hot-electrons will then get injected into the high energy levels (S_n) of the adjacent QDs' conduction band. [32d, 41]

(3) Spontaneous emission enhancement: These injected electrons will non-radiatively decay from a discrete high energy level (S_n) to a lower one (S_{n-1}) within QDs, followed by radiative decay from the energy level (S_{n-1}) to ground state (S_0) with a photon emission ($\hbar\nu_2$).

In the case of $FAPbI_3$ perovskite QDs on a-Sb_2Te_3 nanoantennae (Figure 2g), there are two key differences with respect to the crystalline case. First, the localized surface plasmon resonance for a-

Sb_2Te_3 is much weaker than the corresponding crystalline one (see Figure 2c), and thus it is less efficient at generating hot electron-hole pairs. Second, a-Sb_2Te_3 possesses a disordered lattice structure and does not exhibit the well-defined energy band diagram, preventing it from forming an effective heterojunction with perovskite QDs. Therefore, the dominating light emission mechanism in this system is based on the direct excitation of electron-hole pairs inside perovskite QDs. The excited electrons at the S_2 energy state relax to S_1 non-radiatively, and then recombine with the holes at the ground state (S_0) in $FAPbI_3$ with a photon energy of $\hbar\nu_1$ (1.64 eV).

A control experiment was conducted to validate the proposed mechanism of surface-enhanced Landau damping in the perovskite/c-Sb_2Te_3 quantum emission system. A 10-nm-thick Al_2O_3 insulating layer was deposited on c-Sb_2Te_3 nanoantennae before adding perovskite quantum dots (Supplementary Figure S10). The results support the proposed mechanism, demonstrating that the uncovered c-Sb_2Te_3 nanoantenna facilitates hot-electron excitation via interband plasmonics, and followed by hot-electron injection.

4. Engineering Surface-Enhanced Landau Damping via Geometrical Dimensions

Next, we demonstrate the size-dependence of quantum emission in perovskite/Sb_2Te_3 nanoantennae. **Figure 3a** presents the reflectance spectra of the bare Sb_2Te_3 nanodisk array with a fixed pitch of 420 nm and a height of 150 nm, with varying nanodisk diameters ranging from 280 nm to 380 nm (*i.e.*, the gap size decreasing from 140 nm to 40 nm). The reflectance spectra in **Figure 3a** show that the spectral position of the corresponding plasmonic resonance dips red-shift from 520 nm to 580 nm. In their crystalline state, the nanodisk array exhibits resonant dips that are narrower and more pronounced than the ones in the amorphous a-Sb_2Te_3 nanoantennae. These resonance features are not observed in 150-nm-thick a-Sb_2Te_3 and c-Sb_2Te_3 film (Supplementary Figure S11).

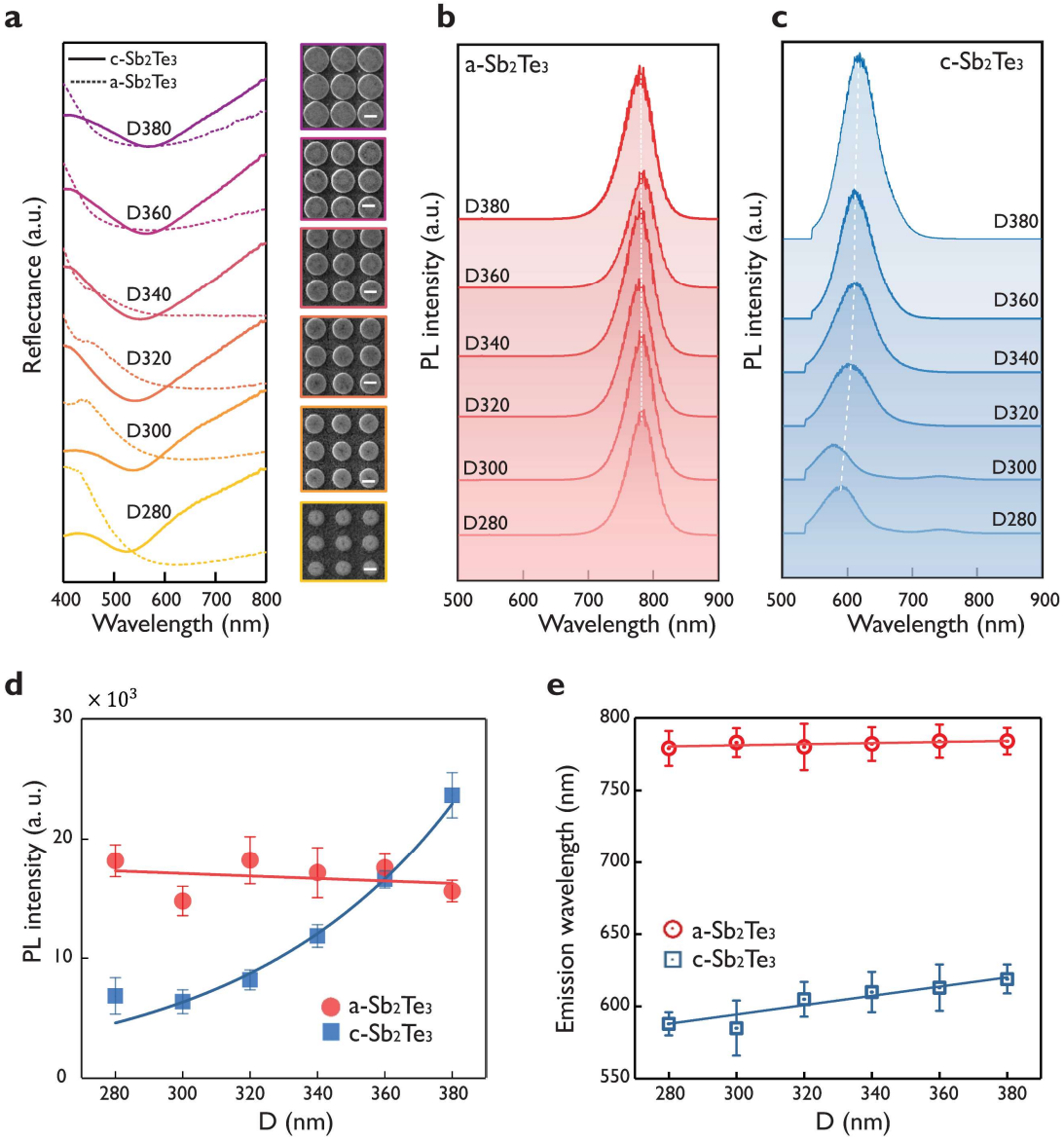

Figure 3 | Engineering surface-enhanced Landau damping via geometrical tuning. a, Reflectance spectra of bare Sb_2Te_3 nanoantenna arrays with a fixed pitch of 420 nm and disk diameters ranging from 280 nm to 380 nm. Corresponding SEM images are shown on the right (scale bar: 200 nm). **b, c**, PL spectra of Sb_2Te_3 nanodisks in amorphous and crystalline states, coated with QDs, showing emission peaks at ~760 nm and ~600 nm, respectively. **d**, Photoluminescence intensity of $FAPbI_3/Sb_2Te_3$ quantum emitters as a function of nanodisk diameter. **e**, Emission wavelength dependence of QDs on c-Sb_2Te_3 and a-Sb_2Te_3 nanoantenna arrays with varying nanodisk diameters.

The PL emission of QDs was recorded on a-Sb_2Te_3 and c-Sb_2Te_3 nanoantennae over a 50 × 50 μm^2 (see the raster scanning PL images in Supplementary Figure S12). As shown in **Figure 3b**, when the nanodisk diameter is increasing, the quantum emissions remained at 755 nm for $FAPbI_3$ QDs on a-Sb_2Te_3 nanoantenna. This is due to the lack of hot-electron injection in form a-Sb_2Te_3 to $FAPbI_3$. In comparison, for $FAPbI_3$ QDs on c-Sb_2Te_3 nanoantennae, the PL emissions energy can be engineered up to a higher level of 2.11 eV (λ=588 nm), as shown in **Figure 3c**. Moreover, since the c-Sb_2Te_3 nanoantennae support a strong localized plasmon resonance (see simulation results in Supplementary Figure S13), it enables the enhancement of PL intensity.

Figures 3d and **3e** show the photoluminescence intensity and peak wavelength of $FAPbI_3$ QDs on Sb_2Te_3 nanoantennae as a function of nanodisk diameters, where the PL spectra were averaged from 20 sites for each nanoantenna region. Figure 3d demonstrates the PL intensity from $FAPbI_3$ QDs on a-Sb_2Te_3 antenna (red solid circles) does not change with the diameter of a-Sb_2Te_3 nanodisk. In comparison, for $FAPbI_3$ QD on c-Sb_2Te_3 (blue solid squares), the effect of LSP excited hot-electrons and their injection at the interface becomes more intense with the diameter increasing (small gap). A mininuim photoluminescence (PL) intensity of $(6.8 \pm 1.5) \times 10^3$ with a enhancement of 5-fold was observed for quantum dots (QDs) deposited on crystalline Sb_2Te_3 (c-Sb_2Te_3) nanoantennae with a diameter of 280 nm and a gap size of 120 nm.

Additionally, a maximum PL intensity of $2.37 \pm 0.19) \times 10^4$ with ~17-fold enhancement was achieved for perovskite QDs deposited on c-Sb_2Te_3 nanoantennae with a diameter of 380 nm and a gap size of 40 nm, compared to the PL measured from unpatterned amorphous Sb_2Te_3 (a-Sb_2Te_3) and c-Sb_2Te_3 film substrates (see Supplementary Figures. S14). In addition, the emission wavelength of $FAPbI_3$ on c-Sb_2Te_3 nanoantenna can be red shifted from 588 nm to 617 nm as shown in Figure 3e, with respect to the diameter of nanodisk increasing from 280 nm to 380 nm (*i.e.*, a gap size reduction to 40 nm). These experimental results show that the dimensions and the gap size of Sb_2Te_3 nanoantennae can control the strength of LSP resonance, which then affects intensity of hot-electron injection and emission

of QDs. On the other hand, on the a-Sb_2Te_3 nanoantenna, the PL emission peak (red open circles in Figure 3e) does not shift significantly since its emission mechanism is determined by the intrinsic characteristics of $FAPbI_3$ QDs itself. Therefore, we present that variation of the Sb_2Te_3 nanoantenna dimensions in its amorphous and crystalline states have significantly different effects on the emitter's PL properties. In particular, the dimensions of a-Sb_2Te_3 nanoantennae have little effect on the QDs' emission wavelength intensity, while the employment of c-Sb_2Te_3 nanoantennae enables a shifting of the quantum emission energy over 360 meV (*i.e.*, from 755 nm to 617 nm), due to the increased electric-field strength supported on the nanodisks.

5. Hybrid plasmonic-Mie resonance for engineering surface-enhanced Landau damping.

Subsequently, we present a method to extend the tunability range of the perovskite QD emission through hybrid nanoantenna designs. Here, by leveraging on the hybrid plasmonic-Mie resonances to minimize system losses, we enhance the Q-factor of the resulting plasmonic features. **Figure 4a** depicts a hybrid antenna design consisting of 130-nm-tall a-Si nanodisks topped with a 50-nm-thick c-Sb_2Te_3 film on top (See *Method 8.2*). The a-Si nanodisk array provides a stable platform for Sb_2Te_3 deposition while simultaneously supporting the desired Mie resonances.[42] Reflectance spectra of hybrid c-Sb_2Te_3/Si and a-Sb_2Te_3/Si nanoantennae are shown in Supplementary Figs. S15 and S16. In both amorphous and crystalline cases, the hybrid resonance mode undergoes a redshift from 600 nm to 723 nm as the nanodisk diameter increases. Notably, the c-Sb_2Te_3/Si hybrid arrays exhibit narrower hybrid resonance dips in the spectra. Compared to bare Sb_2Te_3 arrays (Q factor of ~3.5), hybrid c-Sb_2Te_3/Si arrays with a 50 nm interparticle gap demonstrate a 4-fold increase in the Q factor, reaching value up to ~12, as shown in **Figure 4b**.

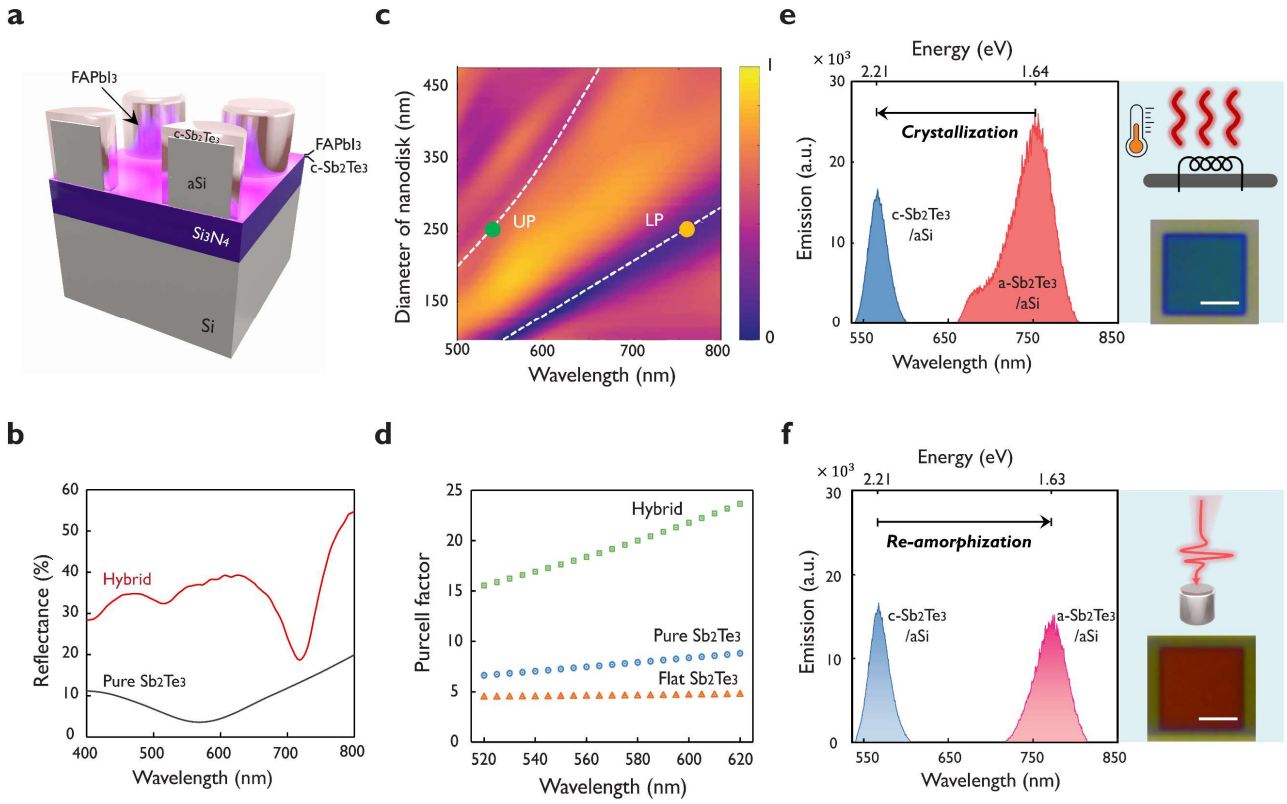

Figure 4 | Tunable energy range via hybrid plasmonic-Mie resonance on c-Sb_2Te_3/a-Si nanoantennae. a, Schematic of a hybrid plasmonic-Mie nanoantenna with $FAPbI_3$ QDs deposited on the surface. **b**, Reflectance spectra of bare c-Sb_2Te_3 (D = 380 nm) and hybrid c-Sb_2Te_3/a-Si nanoantennae (D = 250 nm). **c**, Simulated hybridized optical modes arising from the coupling of interband plasmonic and Mie resonances, with "UP" and "LP" denoting upper and lower polariton modes, respectively. **d**, Simulated Purcell enhancement at 561 nm, showing a 4-fold increase in the hybrid nanoantenna and 1.7-fold increase in the pure Sb_2Te_3 nanoantennae, with respect to the ones on flat Sb_2Te_3 film, respectively. **e**, PL spectra showing a 570 meV blue shift in perovskite QD emission on hybrid Sb_2Te_3/a-Si nanodisks (D = 250 nm) upon the phase transition of Sb_2Te_3 from amorphous to crystalline. **f**, PL spectra of perovskite QDs before and after laser-induced amorphization of the hybrid nanoantenna (scale bar: 15 μm).

The hybridization of two optical modes in the c-Sb_2Te_3/a-Si system was analyzed via FDTD simulations (see *Method 8.5*), as shown in **Figure 4c**. The reflectance spectra reveal two hybridized

modes: the first (yellow dot) corresponds to the plasmon-like upper polariton (UP) mode, while the second (green dot) represents the lower polariton (LP) mode. The corresponding electric field distributions are provided in Supplementary Figure S17. A hybrid nanoantenna with a 250 nm a-Si disk exhibits the coupling effect between the UP and LP mode. We further examined the Purcell effect in the hybrid nanoantennae and bare c-Sb_2Te_3 nanoantennae, when perovskite $FAPbI_3$ quantum emitters are deposited on the nanoantennae, as well as flat c-Sb_2Te_3 film. Theoretically, the Purcell factor can be expressed as:

$$F_p = \frac{3\lambda^3 Q}{4\pi^2 n^3 V_{eff}} \quad (1)$$

where F_p is the Purcell factor, λ is the wavelength in free space, n is the refractive index of cavity material, Q is the quality factor of the resonance and V_{eff} is the effective mode volume. **Figure 4d** presents the simulated Purcell factor for a hybrid nanoantenna (250 nm diameter), a bare c-Sb_2Te_3 nanoantenna (380 nm diameter), and a flat c-Sb_2Te_3 film. Due to the higher Q-factor of the hybrid nanoantenna, simulated Purcell enhancement shows a 4-fold increase in the hybrid nanoantenna and 1.7 times increase in the pure Sb_2Te_3 nanoantennae as compared to the flat Sb_2Te_3 film, at an emission wavelength of 561 nm respectively. To quantify PL enhancement from the Purcell effect, we conducted time-resolved photoluminescence measurements (see *Method 8.4*). Lifetime measurements of perovskite QDs on nanoantennas and flat region are presented in Supplementary Figure S18. The average lifetime of QDs on hybrid nanoantennas is 8.06 ns, significantly shorter than the 13.49 ns observed on a c-Sb_2Te_3 film. Therefore, the radiative decay rate enhancement is ~1.67-fold, where the shorter lifetime for perovskite QDs on c-Sb_2Te_3/aSi nanoantennae indicates a faster spontaneous emission rate, as compared to the ones on the c-Sb_2Te_3 flat region.

A photoluminescence (PL) peak shift exceeding 570 meV was observed when Sb_2Te_3 transitioned from the amorphous to the crystalline state in the hybrid nanoantennae (**Figure 4e**). The inset of Figure 4e presents a microscopy image of the hybrid nanoantennae, appearing bluish after crystallization. The PL intensity at 561 nm increased by approximately 12-fold in c-Sb_2Te_3 nanodisks

compared to perovskite QDs in the off-nanoantennae region of c-Sb_2Te_3 film (Supplementary Figure S14). PL spectra for QDs deposited on samples with disk diameters of 170-250 nm are shown in Supplementary Figure S19. Next, we carry out the FDTD simulations to analyze the enhanced absorption effect of the pump laser, where the pump laser absorption is proportional to the localized optical intensity around the QDs, *i.e.*, $|E/E_{inc}|^2$.[43] It shows that the perovskite QDs on hybrid c-Sb_2Te_3/a-Si nanoantenna is able to achieve ~24-fold enhancement in the pump laser absorption, as compared to the ones on 50-nm-thick flat c-Sb_2Te_3 film with a roughness of 4.2 nm (see Supplementary Figure S20). Therefore, the enhanced PL emission from perovskite QDs on hybrid c-Sb_2Te_3/a-Si antenna is mainly contributed by the increased pump laser absorption, rather than Purcell effect.

A key advantage of integrating Sb_2Te_3 in this hybrid nanoantenna design is its reversible phase transition, enabling dynamic tuning of the PL response in deposited QDs. We demonstrate this reversible emission tuning using a 780 nm femtosecond laser with a scanning speed of 20 μm/s and an incident power of 6.5 mW (See *Method 8.3*) scanning on nanoantennae. Laser scanning induces amorphization of Sb_2Te_3, shifting the PL emission peak back to its original lower-energy position (**Figure 4f**). The inset shows a microscopy image of the hybrid nanoantennae appearing reddish after re-amorphization. The corresponding reflectance spectra upon phase switching are provided Supplementary Figure S21. Thus, the use of hybrid c-Sb_2Te_3/a-Si arrays arrays enable switchable quantum emission.

6. Modulating and controlling of surface-enhanced Landau damping via external DC bias.

The electrical modulation of the hot-electron injection process in hybrid c-Sb_2Te_3/aSi nanoantennae with QDs provides an additional switchable freedom of this quantum emission system. We investigate it by applying an external DC electrical field to control over the hot-electron injection process. **Figure 5a** illustrates the device schematic, which is packaged on a PCB board. The hybrid c-Sb_2Te_3/a-Si nanoantenna with QDs is sandwiched between the bottom electrode (a *p*-type silicon substrate) and an ITO electrode. A 350-nm silicon dioxide (SiO_2) layer serves as an insulating barrier

between the top and bottom electrodes while also encapsulating the $FAPbI_3$/c-Sb_2Te_3/a-Si nanoantennae. During the voltage-dependent PL spectra characterization, the bottom Si substrate was grounded while the top ITO electrode was voltage biased. The electrical modulation of the QDs emission was performed by using a dual-channel source meter. A DC voltage bias was applied on top and bottom electrode of device while monitoring the electrical current readout and recording the PL emission using a spectrometer (see *Method 8.4*). **Figure 5b** presents the measured electrical current (box chart) across the electrodes when a DC bias voltage is applied to the hybrid quantum emitter. The center line inside the box represents the mean current value, while the error bars indicate variations in current at each DC voltage bias. The low electrical current (~ pA) suggests that quantum emission in the hybrid nanoantenna is modulated by the static DC electric field rather than by tunneling current. Under a 4 V bias, the electrical current is $(6.33 \pm 2.30) \times 10^{-1}$ A, which is higher than the $\sim (5.94 \pm 3.05) \times 10^{-11}$ A under a reverse 4 V bias. This discrepancy can be attributed to the hot-electron injection process being enhanced by the static DC electric field.

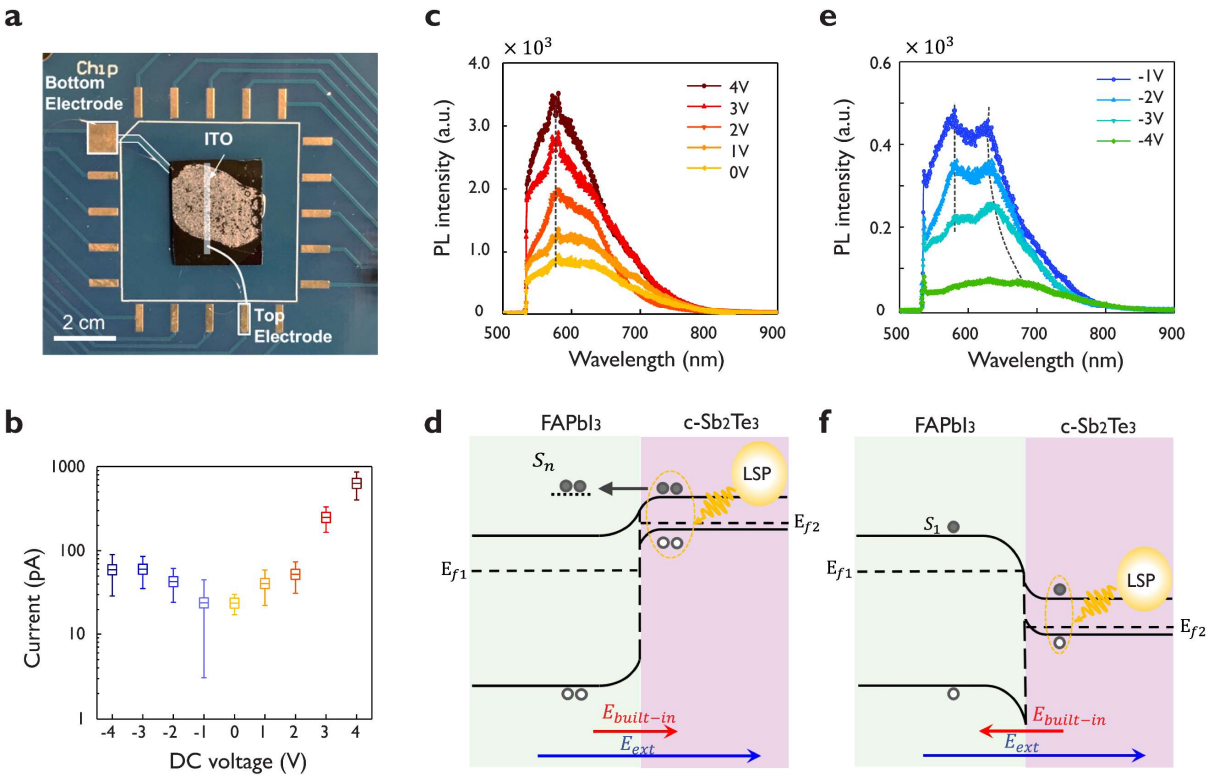

Figure 5 | Electrical modulation of surface-enhanced Landau damping and hot-electron injection process for perovskite QDs on hybrid Sb_2Te_3/a-Si nanoantennae. a, Photograph of electrically modulated nanoantennae under DC bias. **b**, Measured device current between the top and bottom electrodes. **c**, PL spectra under positive DC bias from 0 V to +4 V in 1 V steps. **d**, Schematic energy band diagram illustrating hot-electron injection modulation by a positive bias on the top ITO electrode. **e**, PL spectra under negative DC bias from -1 V to -4 V in 1 V steps. **f**, Schematic energy band diagram under negative bias applied to the top ITO electrode.

Figure 5c presents the PL spectra of hybrid $FAPbI_3$/c-Sb_2Te_3 nanoantennae with a 250-nm disk diameter and 50-nm gap. These spectra were recorded under a positive DC bias voltage condition, increasing from 0V to 4V with a step size of 1V. The intensity of PL spectra increases by 2.7-fold as the positive bias voltage is increased from 0V to 4V. The electrically modulated PL emission wavelength is located at 580 nm. Under the forward bias condition, the external DC static electric field (denoted by $\boldsymbol{E_{ext}}$ with the blue color arrow) facilitates the hot-electron injection process from c-Sb_2Te_3 to $FAPbI_3$ QDs, as compared to the case of zero-bias condition (**Figure 5d**). Therefore, the forward bias voltage will lead to higher intensity of PL spectra.

The negative bias voltage conditions for the excitation process are presented in **Figure 5e**, with the voltage varied from -1 V to -4 V. The main emission peak at 580 nm drops down to 61% of its original PL intensity as the DC voltage bias decreases, indicating a suppression of hot-electron injection process due to the external applied DC field (see the blue arrow of $\boldsymbol{E_{ext}}$). Meanwhile, the second emission peak red shifts from 625 nm to 680 nm (with an emission energy tunable range over 307 meV). Under reverse bias condition, the hot-electron injection is minimized by the opposite direction of external electric field. In this case, the quantum emission is determined by the intrinsic relaxation process of $FAPbI_3$ QDs, as illustrated in **Figure 5f**. Therefore, adjusting the DC voltage from -4V to 4V the PL enables a 22-fold

increase in the PL intensity. The results indicate the hot-electron injection process from c-Sb_2Te_3 to $FAPbI_3$ can be controlled electrically via the external DC bias voltage.

Our results highlighted the advantages of the coupling between phase change Sb_2Te_3 nanoantennae and perovskite QDs in a quantum emission system to achieve controllable and switchable quantum emission. However, complimentary investigations would be beneficial for further analysis on some aspects. For instance, a spatiotemporal ultrafast pump-probe system could be employed to investigate the ultrafast laser-matter interactions in our system,[44] since hot-electron injection is usually at the time scale of ~ femtosecond to picosecond.[42] Meanwhile, the photon relaxation in PL process is in the order of nanosecond.[5a] Therefore, such pump-probe measurement will potentially reveal the decay dynamics of the excited hot electron-hole pairs, and the subsequent injection and decay processes. In addition, determining the breakdown voltage under reverse bias condition would be beneficial in future device design could be studied. Follow-up investigations will involve reversible and programmable switching of the quantum emission from a-Sb_2Te_3 to c-Sb_2Te_3, particularly, by utilising electrical control and switching circuits.

7. Conclusions

This work presents a tunable quantum emission system using a perovskite/Sb_2Te_3 hybrid antennae at ambient condition. The PL emission energy range can be tuned up to 570 meV with an emission enhancement of 12-fold. The underlying mechanism is the excitation of hot electron-hole pairs on the c-Sb_2Te_3 nanostructures and followed by the hot-electron injection into perovskite QDs via the microscopic electron transport process. Moreover, the quantum emission can be electrically modulated on the hybrid nanoantennae using an external DC voltage bias. The change in DC bias voltage from -4 V to 4 V induced a 22-fold enhancement of the quantum emission intensity. The integration of phase-change interband plasmonics with perovskite QDs has demonstrated unprecedented controllability over quantum emission characteristics, offering a versatile platform for tailoring light-matter interactions at

the nanoscale. The tunable quantum emission could be applied to single-photon manipulation in the integrated quantum photonics towards photonic-based quantum computing.

8. Methods

8.1 Nanofabrication of Sb_2Te_3 nanoantenna

A 150 nm phase change material Sb_2Te_3 was deposited on a 70-nm-thick Si_3N_4/ Si substrate by using radio frequency (RF) sputtering. The film was deposited from a 2-inch diameter, 0.125-inch thick Sb_2Te_3 target (purity > 99.9%) with power of 20 W, pressure of 0.5 Pa, and Ar gas ambient in the main chamber at room temperature. The deposition rate is around 4.725 nm/min. And as-deposited Sb_2Te_3 film is amorphous state. A thin layer (~80 nm) of Hydrogen silsesquioxane (HSQ) as an electron beam resist mask was spined coating on top of the $Sb_2Te_3/Si_3N_4/Si$ substrate and exposed by using electron beam lithography (EBL, Elionix ELS-7000). The electron beam current of 500 pA and an exposure dose of ~ 12 mC/cm^2. The sample was then developed by a NaOH/NaCl salty solution (1% wt/ 4% wt in deionized water) for 60 s and rinsed by deionized water for another 60 seconds to stop the development. Then the sample was rinsed by acetone and isopropanol alcohol (IPA) and dried with nitrogen gas blow. With HSQ as an etching mask, Sb_2Te_3 film nanodisk array etching was carried by ICP (Oxford Plasmalab 100 - Cobra) with a radio frequency power of 200W, ICP power of 600 W, HBr gas flow rate of 7.5 sccm (standard cubic centimeter per minute) and Ar gas flow rate of 22.5 sccm, under a process pressure of 5 mTorr, and at temperature of 40 °C in the main chamber. The total etching time is 15 seconds. The Si_3N_4 film acts an etching stop layer due to the large selectivity of etching rates between Sb_2Te_3 and Si_3N_4. With an annealing condition of 180 °C for 15 minutes in the furnace, the lattice structure of Sb_2Te_3 can be switched from an amorphous to a crystalline state.

8.2 Nanofabrication of hybrid Sb_2Te_3-aSi nanoantenna

A 130-nm-thick amorphous silicon (aSi) was grown on 70-nm-thick Si_3N_4/Si substrate using the plasma-enhanced chemical vapor deposition (PECVD) method. A thin layer (~30 nm) of hydrogen silsesquioxane (HSQ) as a photo mask was a spined coating on top of the silicon substrate and exposed by using electron beam lithography (EBL, Elionix ELS-7000). The beam current of 500 pA and an exposure dose of ~ 12 mC/cm^2. The photo-resist development process flow is the same as in the previous bare Sb_2Te_3 nanoantenna. A 130-nm-thick aSi nanodisks dry etching was carried out by ICP (Oxford Instruments, Plasmalab System 100), with a radio frequency power of 100 W, ICP power of 150 W, Cl_2 gas flow rate of 22 sccm, under a process pressure of 5 mTorr, and temperature of 0°C in the main chamber. After that, a 50-nm-thick Sb_2Te_3 film layer was deposited on top of aSi nanodisk array using radio frequency (RF) sputtering with a conformal step coverage. To achieve Sb_2Te_3-aSi nanoantenna, the annealing process is as the same as the one for bare Sb_2Te_3 nanoantenna. Regarding to hybrid nanoantenna for electrically modulation, a 350 nm SiO_2 insulator film was deposited on hybrid c-Sb_2Te_3/aSi nanoantenna by using radio frequency (RF) sputtering system. Then 300 nm ITO top electrode strip was patterned on top of SiO_2 film by lithography and lift-off process.

8.3 Femtosecond Laser-Induced Crystalline-to-Amorphous Transition

The crystalline state of the c-Sb_2Te_3 sample can be transitioned to an amorphous state using a femtosecond laser.[17a] This laser-induced amorphization process was performed employing the Nanoscribe GmbH Photonic Professional GT system, equipped with a femtosecond fiber laser operating at a central wavelength of 780 nm. The laser source delivers a total power of 50 mW, with pulse lengths ranging between 100 fs and 200 fs. During the laser-induced amorphization process, 13% of the total laser power was utilized, corresponding to 6.5 mW, while employing a scanning speed of 20 μm/s. The hatching distance during laser scanning was maintained at 200 nm. Notably, a 40× Olympus objective with a numerical aperture (NA) of 0.75 was employed throughout the experimentation.

8.4 Optical characterizations

(1) Reflectance measurements were carried out using a polarized broadband white light source on a CRAIC UV-vis-NIR micro-spectrophotometer equipped with a 5× objective lens (NA=0.12). The measurements were calibrated using a National Institute of Standards and Technology (NIST) calibration sample (Enhanced aluminum mirror) to calculate the absolute reflectance of the nanoantenna and operated with an integration time of 100 ms with an average of 25 measurements per spectrum. (2) The PL measurement of quantum emission was carried out at room temperature unless otherwise stated. Before annealing process, the perovskite QDs dissolved in toluene solution was dropped cast on bare a-Sb_2Te_3 and hybrid a-Sb_2Te_3/aSi nanoantenna array for PL measurements, respectively. After PL characterization, the perovskite QDs on the nanoantenna samples had been cleaned by toluene solution thoroughly. Followed by annealing process of nanoantenna samples, PL measurement was carried out again with perovskite QDs dropping cast on nanoantenna samples with c-Sb_2Te_3 film. Prior to drop casting the $FAPbI_3$ quantum dots onto the sample surface, the nanoparticles were purified by size using a centrifuge to remove any aggregation. PL mapping measurements on each nanoantenna with different dimensions were collected with laser spot scanning pixel by pixel. The spectra were extracted and averaged by 5-sites of each block. The PL mapping was conducted on a WITec Alpha 300 S Optical Microscope in confocal mode. A linearly polarized 532 nm CW laser with a power of 100 μW was focused on the sample through a 50× objective with a NA of 0.6. The integration time is 0.05 seconds. (3) The electrically modulated PL spectra are performed using a computer-controlled dual-channel sourcemeter (Keithley 2636B) for simultaneous application of a DC voltage and readout of device electric current and WITec Alpha 300 S Scanning Near-field Optical Microscope equipped with a micro-spectrometer. When the DC voltage bias applied on the nanoantenna with QDs between top electrode ITO and bottom Si substrate, the spectra were recorded by spectrometer through measuring the photon emission intensity in image scanning mode. Five-site with a scanning area of 3μm×3μm including 12500 (sample size) PL spectra were recorded and averaged under a particular DC voltage bias varying from -4V to 4V. During the electrically modulated PL measurement on hybrid nanoantenna with quantum

emitters, the input power of laser has been tuned up to 1.7 mW and integration time has been increased to 0.5 seconds to get a better signal-to-noise ratio.

(4) Lifetime measurements were carried out using a home-built confocal microscope setup at room temperature. In the setup, a 515 nm pump laser (Omicron) was scanned by a 15-steering mirror system (Newport) and focused onto the sample via a 4f lens system and a 100× microscope objective (Olympus, NA = 0.9). The lifetime measurements were conducted with the 515 nm laser operating in pulsed mode (110 ps pulse duration, 2 MHz repetition rate), while emitted photons were detected using a single-photon avalanche diode (SPAD) (Excelitas). Temporal correlations between the SPAD-detected emission and laser pulses were measured with a time-to-digital converter (QuTools quTau) at an 81 ps resolution. Spectral filtering was applied using a Semrock 732/68 bandpass filter.

8.5 Numerical simulations

The far-field spectra and the near-field distributions were obtained using 3D finite-difference time-domain (3D-FDTD) simulations with Lumerical FDTD Solutions software. Typically, in bare Sb_2Te_3 nanodisk arrays, it was placed in a 300 nm × 300 nm × 1500 nm unit cell with a 4 nm × 4 nm × 4 nm mesh around them. The unit cell had a perfectly matched layer (PML) in the *z* direction and periodic boundary conditions in the x and y directions. The reflectance spectrum was recorded at normal incidence condition by a monitor placed above a plane wave source, with the polarization of the incident light wave set to be along the x- or y-axis. The refractive index (*n*) and extinction coefficient (*k*) values of Sb_2Te_3 were taken from ellipsometry measurements (See Supplementary Figure 5, 6 and 7). The Purcell factor calculation was carried out using the built-in calculation method of the software, using the ratio of the dipole emission power over the total emitted energy. The PML boundary conditions limit the calculation domain. The point dipole source was placed onto a 20 × 20 array of the nanodisks array at the highest electric field enhancement of a nanodisk edge. A point electric dipole source representing the quantum emitter was placed at the location of the highest field enhancement on the edge of the top

surface of the nanodisk. The electric dipole emission wavelength was set at 755 nm with a 100 nm span, and *Fp* was obtained by averaging the results from the orthogonal dipole orientations (*x*-, *y*-, and *z*-polarizations) at different positions including base, corner and top on nanodisk structures.

Supporting Information

Supporting Information is available from the Wiley Online Library or from the author.

Acknowledgments

Z.D. would like to acknowledge the funding support from the Agency for Science, Technology and Research (A*STAR) under its AME IRG (Project No. A20E5c0093), Career Development Award grant (Project No. C210112019), MTC IRG (Project No. M21K2c0116 and M22K2c0088), the Quantum Engineering Programme 2.0 (Award No. NRF2021-QEP2-03-P09), DELTA-Q 2.0 (Project No. C230917005) and National Research Foundation via Grant No. NRF-CRP30-2023-0003. J.K.W.Y. would like to acknowledge the funding support from National Research Funding (NRF) Singapore NRF-CRP20-2017-0001 and NRF-NRFI06-2020-0005. C.-W.Q. would like to acknowledge the funding support from the Competitive Research Program Award (NRF-CRP22-2019-0006 & NRF-CRP26-2021-0004) from the NRF, Prime Minister's Office, Singapore, and by a grant (A-0005947-16-00) from Advanced Research and Technology Innovation Centre (ARTIC), National University of Singapore. N.A.M. would like to acknowledge the funding support from the Danish National Research Foundation (Project No.~DNRF165). We also would like to thank Dr. Shengyuan A. Yang from Research Laboratory for Quantum Materials, IAPME, Faculty of Science and Technology, University of Macau, Macau SAR who has kindly supported for this work in energy band diagram calculation by Density Functional Theory.

Received: ((will be filled in by the editorial staff))
Revised: ((will be filled in by the editorial staff))
Published online: ((will be filled in by the editorial staff)

Authors' contributions

Z.D. and J.K.W.Y. conceived the concept, designed the experiments, and supervised the project. Y.L. wrote the manuscript with the inputs from Z.D. and J.K.W.Y. Y.L., J.Z., S.L.K.Y., H.Y.L.L., W.P.G. and Z.D. did the nanofabrication of the nanostructures. N.Q.A. and R.E.S. performed the material deposition. Z.Z. performed XPS material characterizations. Y.L., E.C. and S.Z. performed the photoluminescence spectra characterizations. D.A.K. carried time-resolved photoluminescence spectra measurement. H. W. performed Crystalline-to-Amorphous switching by femtosecond laser. H.Y.L.L. carried out the SEM imaging. Y.L. performed the finite-difference time-domain (FDTD) simulations. L.J.L and Z.-K.T. synthesis and characterized the perovskite quantum dots. J.R.S., and L.L.X. performed density function theory calculation. N.A.M., R.E.S., and C.-W.Q. participated in discussions and provided suggestions to improve the quality of the manuscript. All authors analyzed the data, read, and corrected the manuscript before the submission.

Competing interests

The authors declare no competing interests.

Supplementary information

Supporting Information is available from the Wiley Online Library.

References

[1] N. Ahn, C. Livache, V. Pinchetti, H. Jung, H. Jin, D. Hahm, Y.-S. Park, V. I. Klimov, *Nature* **2023**, 617, 79.
[2] H. Wang, H. Wang, Q. Ruan, J. Y. E. Chan, W. Zhang, H. Liu, S. D. Rezaei, J. Trisno, C.-W. Qiu, M. Gu, J. K. W. Yang, *Nature Nanotechnology* **2023**, 18, 264.
[3] Y. Chen, J. Feng, Y. Huang, W. Chen, R. Su, S. Ghosh, Y. Hou, Q. Xiong, C.-W. Qiu, *Nature Materials* **2023**, 22, 1065.
[4] a)Z. Dong, L. Jin, S. D. Rezaei, H. Wang, Y. Chen, F. Tjiptoharsono, J. Ho, S. Gorelik, R. J. H. Ng, Q. Ruan, C.-W. Qiu, J. K. W. Yang, *Science Advances* **2022**, 8, eabm4512; b)Y. H. Fu, A. I. Kuznetsov, A. E. Miroshnichenko, Y. F. Yu, B. Luk'yanchuk, *Nature Communications* **2013**, 4, 1527; c)J. Ho, Y. H. Fu, Z. Dong, R. Paniagua-Dominguez, E. H. H. Koay, Y. F. Yu, V. Valuckas, A. I. Kuznetsov, J. K. W. Yang, *ACS Nano* **2018**, 12, 8616.
[5] a)E. Csányi, Y. Liu, S. D. Rezaei, H. Y. L. Lee, F. Tjiptoharsono, Z. Mahfoud, S. Gorelik, X. Zhao, L. J. Lim, D. Zhu, J. Wu, K. E. J. Goh, W. Gao, Z.-K. Tan, G. Leggett, C.-W. Qiu, Z. Dong, *Advanced Functional Materials* **2024**, 34, 2309539; b)J. Tian, Q. Y. Tan, Y. Wang, Y. Yang, G. Yuan, G. Adamo, C. Soci, *Nature Communications* **2023**, 14, 1433.
[6] C. He, Y. Shen, A. Forbes, *Light: Science & Applications* **2022**, 11, 205.
[7] J. Wang, F. Sciarrino, A. Laing, M. G. Thompson, *Nature Photonics* **2020**, 14, 273.
[8] Z. H. Peng, S. E. de Graaf, J. S. Tsai, O. V. Astafiev, *Nature Communications* **2016**, 7, 12588.
[9] M. Spagnolo, J. Morris, S. Piacentini, M. Antesberger, F. Massa, A. Crespi, F. Ceccarelli, R. Osellame, P. Walther, *Nature Photonics* **2022**, 16, 318.
[10] C. Feng, B.-W. Li, Y. Dong, X.-D. Chen, Y. Zheng, Z.-H. Wang, H.-B. Lin, W. Jiang, S.-C. Zhang, C.-W. Zou, G.-C. Guo, F.-W. Sun, *Science Advances* **2023**, 9, eadg9376.
[11] a)J. Carolan, C. Harrold, C. Sparrow, E. Martín-López, N. J. Russell, J. W. Silverstone, P. J. Shadbolt, N. Matsuda, M. Oguma, M. Itoh, G. D. Marshall, M. G. Thompson, J. C. F. Matthews, T. Hashimoto, J. L. O'Brien, A. Laing, *Science* **2015**, 349, 711; b)P. J. Shadbolt, M. R. Verde, A. Peruzzo, A. Politi, A. Laing, M. Lobino, J. C. F. Matthews, M. G. Thompson, J. L. O'Brien, *Nature Photonics* **2012**, 6, 45.
[12] M. Förtsch, J. U. Fürst, C. Wittmann, D. Strekalov, A. Aiello, M. V. Chekhova, C. Silberhorn, G. Leuchs, C. Marquardt, *Nature Communications* **2013**, 4, 1818.
[13] X. Xue, N. Calabretta, *Nature Communications* **2022**, 13, 2257.
[14] a)K. Xia, F. Sardi, C. Sauerzapf, T. Kornher, H.-W. Becker, Z. Kis, L. Kovacs, D. Dertli, J. Foglszinger, R. Kolesov, J. Wrachtrup, *Optica* **2022**, 9, 445; b)I.-C. Benea-Chelmus, S. Mason, M. L. Meretska, D. L. Elder, D. Kazakov, A. Shams-Ansari, L. R. Dalton, F. Capasso, *Nature Communications* **2022**, 13, 3170.
[15] a)J. Tian, G. Adamo, H. Liu, M. Wu, M. Klein, J. Deng, N. S. S. Ang, R. Paniagua-Domínguez, H. Liu, A. I. Kuznetsov, C. Soci, *Advanced Materials* **2023**, 35, 2207430; b)C. Choi, S.-E. Mun, J. Sung, K. Choi, S.-Y. Lee, B. Lee, *Advanced Functional Materials* **2021**, 31, 2007210.
[16] Z. Zhang, S. Ghimire, T. Okamoto, B. M. Sachith, J. Sobhanan, C. Subrahmanyam, V. Biju, *ACS Nano* **2022**, 16, 160.
[17] a)L. Lu, Z. Dong, F. Tijiptoharsono, R. J. H. Ng, H. Wang, S. D. Rezaei, Y. Wang, H. S. Leong, P. C. Lim, J. K. W. Yang, R. E. Simpson, *ACS Nano* **2021**, 15, 19722; b)O. A. M. Abdelraouf, A. P. Anthur, Z. Dong, H. Liu, Q. Wang, L. Krivitsky, X. Renshaw Wang, Q. J. Wang, H. Liu, *Advanced Functional Materials* **2021**, 31, 2170356; c)X. Sha, K. Du, Y. Zeng, F. Lai, J. Yin, H. Zhang, B. Song, J. Han, S. Xiao, Y. Kivshar, Q. Song, *Science Advances* **2024**, 10, eadn9017.
[18] W. Ma, T. Wu, N. Yao, W. Zhou, L. Jiang, Q. Qiu, J. Li, Z. Huang, *Communications Materials* **2022**, 3, 68.
[19] M. Zhu, M. Xia, F. Rao, X. Li, L. Wu, X. Ji, S. Lv, Z. Song, S. Feng, H. Sun, S. Zhang, *Nature Communications* **2014**, 5, 4086.

[20] Y. Sun, H. Qin, C. Zhang, H. Wu, L. Yin, Z. Liu, S. Guo, Q. Zhang, W. Cai, H. Wu, F. Guo, J. Sui, *Nano Energy* **2023**, 107, 108176.
[21] N. S. Mueller, R. Arul, G. Kang, A. P. Saunders, A. C. Johnson, A. Sánchez-Iglesias, S. Hu, L. A. Jakob, J. Bar-David, B. de Nijs, L. M. Liz-Marzán, F. Liu, J. J. Baumberg, *Nature Communications* **2023**, 14, 5726.
[22] A. Campos, N. Troc, E. Cottancin, M. Pellarin, H.-C. Weissker, J. Lermé, M. Kociak, M. Hillenkamp, *Nature Physics* **2019**, 15, 275.
[23] K. V. Sreekanth, R. Medwal, C. M. Das, M. Gupta, M. Mishra, K.-T. Yong, R. S. Rawat, R. Singh, *Nano Letters* **2021**, 21, 4044.
[24] H. Zhang, C.-X. Liu, X.-L. Qi, X. Dai, Z. Fang, S.-C. Zhang, *Nature Physics* **2009**, 5, 438.
[25] I. Mohelsky, J. Wyzula, F. Le Mardelé, F. Abadizaman, O. Caha, A. Dubroka, X. D. Sun, C. W. Cho, B. A. Piot, M. F. Tanzim, I. Aguilera, G. Bauer, G. Springholz, M. Orlita, *Physical Review B* **2024**, 109, 165205.
[26] J.-Y. Ou, J.-K. So, G. Adamo, A. Sulaev, L. Wang, N. I. Zheludev, *Nature Communications* **2014**, 5, 5139.
[27] a)M. Zhao, M. Bosman, M. Danesh, M. Zeng, P. Song, Y. Darma, A. Rusydi, H. Lin, C.-W. Qiu, K. P. Loh, *Nano Letters* **2015**, 15, 8331; b)H. Chen, H. Liu, Z. Zhang, K. Hu, X. Fang, *Advanced Materials* **2016**, 28, 403; c)S. G. Menabde, J. T. Heiden, V. A. Zenin, N. A. Mortensen, M. S. Jang, *Advanced Optical Materials* **2024**, 12, 2302797.
[28] N. Talebi, C. Ozsoy-Keskinbora, H. M. Benia, K. Kern, C. T. Koch, P. A. van Aken, *ACS Nano* **2016**, 10, 6988.
[29] a)B. Zhao, M. Vasilopoulou, A. Fakharuddin, F. Gao, A. R. b. Mohd Yusoff, R. H. Friend, D. Di, *Nature Nanotechnology* **2023**, 18, 981; b)Y. Fu, H. Zhu, J. Chen, M. P. Hautzinger, X. Y. Zhu, S. Jin, *Nature Reviews Materials* **2019**, 4, 169.
[30] S. S. Mali, J. V. Patil, J.-Y. Shao, Y.-W. Zhong, S. R. Rondiya, N. Y. Dzade, C. K. Hong, *Nature Energy* **2023**, 8, 989.
[31] L. Protesescu, S. Yakunin, S. Kumar, J. Bär, F. Bertolotti, N. Masciocchi, A. Guagliardi, M. Grotevent, I. Shorubalko, M. I. Bodnarchuk, C.-J. Shih, M. V. Kovalenko, *ACS Nano* **2017**, 11, 3119.
[32] a)C. Clavero, *Nature Photonics* **2014**, 8, 95; b)M. L. Brongersma, N. J. Halas, P. Nordlander, *Nature Nanotechnology* **2015**, 10, 25; c)K. Wu, H. Zhu, Z. Liu, W. Rodríguez-Córdoba, T. Lian, *Journal of the American Chemical Society* **2012**, 134, 10337; d)K. Wu, W. E. Rodríguez-Córdoba, Y. Yang, T. Lian, *Nano Letters* **2013**, 13, 5255.
[33] Y. Wang, P. Landreman, D. Schoen, K. Okabe, A. Marshall, U. Celano, H. S. P. Wong, J. Park, M. L. Brongersma, *Nature Nanotechnology* **2021**, 16, 667.
[34] a)J. Toudert, R. Serna, *Opt. Mater. Express* **2016**, 6, 2434; b)J. Toudert, R. Serna, *Opt. Mater. Express* **2017**, 7, 2299.
[35] a)Z. Wang, Z. Dong, Y. Gu, Y.-H. Chang, L. Zhang, L.-J. Li, W. Zhao, G. Eda, W. Zhang, G. Grinblat, S. A. Maier, J. K. W. Yang, C.-W. Qiu, A. T. S. Wee, *Nature Communications* **2016**, 7, 11283; b)S. J. Barrow, X. Wei, J. S. Baldauf, A. M. Funston, P. Mulvaney, *Nature Communications* **2012**, 3, 1275; c)D. I. Yakubovsky, D. V. Grudinin, G. A. Ermolaev, K. Voronin, D. A. Svintsov, A. A. Vyshnevyy, M. S. Mironov, A. V. Arsenin, V. S. Volkov, *Nano Letters* **2023**, 23, 9461.
[36] R. H. Siddique, J. Mertens, H. Hölscher, S. Vignolini, *Light: Science & Applications* **2017**, 6, e17015.
[37] Y. Xu, X. Wang, W. Zhang, L. Schäfer, J. Reindl, F. vom Bruch, Y. Zhou, V. Evang, J.-J. Wang, V. L. Deringer, E. Ma, M. Wuttig, R. Mazzarello, *Advanced Materials* **2021**, 33, 2006221.
[38] J. Yang, S. Mukherjee, S. Lehmann, F. Krahl, X. Wang, P. Potapov, A. Lubk, T. Ritschel, J. Geck, K. Nielsch, *Small* **2024**, 20, 2306350.
[39] E. H. Alizade, *Optics and Spectroscopy* **2022**, 130.
[40] X. Huang, H. Li, C. Zhang, S. Tan, Z. Chen, L. Chen, Z. Lu, X. Wang, M. Xiao, *Nature Communications* **2019**, 10, 1163.

[41] a)A. M. Brown, R. Sundararaman, P. Narang, W. A. Goddard, III, H. A. Atwater, *ACS Nano* **2016**, 10, 957; b)A. Manjavacas, J. G. Liu, V. Kulkarni, P. Nordlander, *ACS Nano* **2014**, 8, 7630.
[42] Y. Kivshar, *Nano Letters* **2022**, 22, 3513.
[43] Z. Dong, S. Gorelik, R. Paniagua-Dominguez, J. Yik, J. Ho, F. Tjiptoharsono, E. Lassalle, S. D. Rezaei, D. C. J. Neo, P. Bai, A. I. Kuznetsov, J. K. W. Yang, *Nano Letters* **2021**, 21, 4853.
[44] M. Segovia, X. Xu, *Nano Letters* **2021**, 21, 7228.